Depth dependent local structures in thin films unraveled by grazing incidence x-ray absorption spectroscopy

Narcizo M. Souza-Neto, Aline Y. Ramos, Hélio C. N. Tolentino, Alessandro
Martins, Antonio D. Santos

HAL Id: hal-00443710

https://hal.science/hal-00443710

Submitted on 4 Jan 2010

Depth dependent local structures in thin films unraveled by grazing incidence x-ray absorption spectroscopy

NARCIZO M. SOUZA-NETO,[a,b][1] ALINE Y. RAMOS,[c,a] HÉLIO C. N. TOLENTINO,[c,a] ALESSANDRO MARTINS[d] AND ANTONIO D. SANTOS[b]

[a]*Laboratório Nacional de Luz Síncrotron, LNLS, CP6192, 13084-971, Campinas, SP, Brazil,* [b]*Departamento de Física dos Materiais e Mecânica, Instituto de Física, Universidade de São Paulo, São Paulo, Brazil,* [c]*Institut Néel, CNRS et Université Joseph Fourier, BP 166, F-38042 Grenoble Cedex 9, France, and* [d]*Universidade Federal de Goiás, Campus Jataí, Jataí, Brazil*

Abstract

A method of using X-ray absorption spectroscopy (XAS) together with resolved grazing incidence geometry for depth profiling atomic, electronic or chemical local structures in thin films is presented. The quantitative deconvolution of thickness-dependent spectral features is performed by fully considering both scattering and absorption formalisms. Surface oxidation and local structural depth profiles in nanometric FePt films are determined, exemplifying the application of the method.

---

[1] Present address: Advanced Photon Source, Argonne National Laboratory, Argonne, Illinois 60439, USA

1. Introduction

Magnetic thin films have attracted a lot of attention due to their extremely high-density magnetic recording applications (Weller & Doemer, 2000). In this regard, a clear understanding of the macroscopic magnetic properties requires a substantial knowledge of its dependence with layers thicknesses (Johnson *et al.*, 1996) and the complex microstructural effects frequently localized at the interface with the substrate or the surface of the films. Such effects can be studied using experimental techniques able to peer selectively in the depth of the films. In a previous letter (Souza-Neto *et al.*, 2006) we presented qualitative results using x-ray absorption spectroscopy (XAS) with resolved grazing incidence (GI) to clarify the thickness-dependent magnetic properties in nanometric CoPt films. A depth dependent chemical order was revealed and the magnetic behavior was interpreted within this framework. In the present paper we provide a rigorous quantitative method for the deconvolution of the local atomic, chemical and magnetic structural depth profiles. This method is then illustrated by its application to oxidized FePt thin films (Martins *et al.*, 2006). The proposed approach makes GI-XAS a unique tool to address the depth dependence of the local structural parameters, suitable for nanometric structures where this dependence is a crucial issue. Moreover, this method provides a new venue to rigorously determine depth dependent electronic structure profiles using XANES (x-ray absorption near edge structure), which turns out to be crucial in understanding striking artifical interface materials (Souza-Neto *et al.*, 2009; Chakalian *et al.*, 2007).

Although the general phenomena of scattering and absorption of x-rays by condensed matter are nowadays quite well understood (Als-Nielsen & McMorrow, 2001), they still are normally explored from unconnected viewpoints. A few well established techniques surpass this general rule with interconnected scattering and absorption techniques, providing invaluable additional selectivity compared to each approach used separately. DAFS (diffraction anomalous fine structure) gives site selectivity and local structural information (Stragier *et al.*, 1992). XAFS (x-ray absorption fine structure) extracted from reflectivity data gives local structural

information from surfaces and interfaces (Keil *et al.*, 2005; Heald *et al.*, 1988; Borthen & Strehblow, 1995). XSW (x-ray standing wave) locates impurities in bulk crystals and nanostructures using an interference field that provides spatial dependence to the x-ray spectroscopic yields from atoms within the field (Bedzyk *et al.*, 1989). Similarly, glacing-incidence x-ray fluorescence (GIXRF) is a sensitive probe of chemical composition as a function of depth (deBoer, 1991). These techniques are based on similar approaches to the one presented here, however they are often tied-up to near-perfect crystal structures or require specific geometries which are not always easily attainable.

We present here a method to extract the structural and electronic or chemical information from X-ray absorption spectra combined with resolved grazing incidence geometry, for accurate depth profiling. Our method is of general application to either reflection and fluorescence detection schemes and the formalism is free of approximations. It takes into account the overall behavior of the real and imaginary parts involved in the photon-matter interaction. It can be directly applied for relatively smooth surfaces with roughness limited to a few nm, where no specific treatment of the roughness is needed. For rougher surfaces it would be necessary include a model for the roughness or to resort to DWBA based methods, as the one developed by Keil *el al* for reflection mode EXAFS (Keil & Lutzenkirchen-Hecht, 2009). The fluorescence yield detection is used here because it offers a much greater sensitivity to surface effects, a better signal to noise and less spurious distortion.

2. Grazing incidence x-ray absorption spectroscopy

X-ray absorption spectra contain information about the ground state of the selected element in a material (local symmetry, oxidation and spin states, spin-orbit coupling in the $2p$ and $3d$ orbitals, crystal field, covalence and charge transfer). As a matter of fact, in the case of $3d$ transition metals essentially structural information is obtained from the K edges, while more magnetic and electronic information is usually deduced from $L_{2,3}$ edge. XAS is not a surface

technique by itself, since the atenuation length of hard x-rays is of a few micrometers in any material. However, in the grazing incidence geometry near the critical angle for total reflection, the x-ray beam is confined within a few nanometers from the surface. For film studies, this confinement has the considerable advantage of minimizing the substrate contribution.

The grazing incidence x-ray absorption measurements were performed at the Brazilian Synchrotron Light Laboratory (LNLS - Laboratório Nacional de Luz Síncrotron). The setup includes 20 μm-vertical slits limiting the beam size on the sample mounted on a high precision goniometer. XANES spectra were collected in the fluorescence mode at the D04B-XAFS1 beamline (Tolentino *et al.*, 2001) with a Si (111) channel-cut monochromator. The incident beam intensity was monitored using a first ion-chamber. The reflected beam and fluorescence emission were simultaneously collected using a second ion-chamber and a 15-elements Ge detector, respectively. The fluorescence emission and x-ray reflectivity curves were used to calibrate and select with an accuracy of $\approx 0.01^o$ the working grazing angle corresponding to a chosen penetration depth profile. For an accurate energy calibration, the transmission through an Iron metal reference foil was monitored using a third ion-chamber.

The collected absorption spectra measured by the fluorescence yield is a mix of contributions coming from different depths. To get quantitative information we must deconvolve them into their absorption contributions from each depth (z) into the films at each photon energy (E) and grazing angle (θ). The electromagnetic radiation amplitude at each set of (E, θ, z) must be known to weightly sum the absorption contributions as function of energy and angle ($\mu_{exp}(E, \theta)$), as follows:

$$\mu_{exp}(E, \theta) = \frac{1}{\Gamma} \int_0^\infty I(E, z, \theta) \mu(E, z) dz \tag{1}$$

where $I(E, z, \theta)$ is the radiation intensity as function of E, z and θ; $\mu(E, z)$ is the absorption spectrum contribution at the depth z and Γ is the normalizing factor $\int_0^\infty I(E, z, \theta) dz$. The main difficulty to determine each $\mu(E, z)$ by solving this equation is the initial calculation of $I(E, z, \theta)$, which depends on how the layers structure of the film dynamically refract and

reflect the incident radiation, as a function of energy and depth. The formalism adopted to determine this intensity and the way to extract the depth dependence from GI-XAS spectra are described in the following section.

2.1. Refracted and reflected amplitudes as a function of the penetration depth, photon energy and incident angle

Several approaches (Born & Wolf, 1993; Henke *et al.*, 1993; Yun & Bloch, 1990; Mikulík, 1997; Als-Nielsen & McMorrow, 2001; deBoer, 1991; Authier, 2001; Baron, 1995; Stepanov *et al.*, 1998; Lee *et al.*, 2003; Parrat, 1954) can be used to estimate the transmissivity of x-rays inside a material. Those based on the dynamical diffraction theory give the most accurate results near the critical angle of total external reflection. We deal here with conditions near the critical energy and angle for absorption and reflectivity resonances. Hence the method must include all dynamical reflections and refractions conditions to determine the internal electromagnetic wave amplitude in the samples. To fulfill these requirements we apply an approach analogous to the recursive Parrat's reflectivity method (Parrat, 1954) to calculate the refracted and reflected amplitudes at every depth within a film formed by n layers, each one with different chemical contributions.

Following the definitions by (Parrat, 1954), we consider an electromagnetic wave propagating into a material:

$$\vec{E} = \vec{E}_0 e^{i[\hat{n}(\vec{k}\cdot\vec{r})-\omega t]} = \vec{E}_0 e^{i[(1-\delta)(\vec{k}\cdot\vec{r})-\omega t]} e^{-\beta(\vec{k}\cdot\vec{r})} \tag{2}$$

where δ and β are the real and imaginary part of the complex refraction index (Als-Nielsen & McMorrow, 2001; Henke *et al.*, 1993; Chantler, 2000) $\hat{n} = 1 - \delta - i\beta$.

The continuity at each interface between the media n and $n-1$ of a film with N layers gives the twin equation :

$$a_{n-1}E_{n-1} + a_{n-1}^{-1}E_{n-1}^R \;\; = \;\; a_n^{-1}E_n + a_nE_n^R \tag{3}$$

$$\left(a_{n-1}E_{n-1} + a_{n-1}^{-1}E_{n-1}^R\right)f_{n-1}k_1 \;\; = \;\; \left(a_n^{-1}E_n + a_nE_n^R\right)f_nk_1$$

where $f_n = (\theta_n^2 - 2\delta_n - 2i\beta_n)^{1/2}$ for each n media and $a_n = e^{-i\frac{\pi}{\lambda}f_n d_n}$ is a phase factor taking into account the absorption, where d_n is the half penetration in the media n. E_n and E_n^R are the total and reflected electric field amplitudes in the media n. The solution of the equation 3 for the reflected amplitude $R_{n-1,n}$ can be recursively determined by

$$R_{n-1,n} = a_{n-1}^4 \left[\frac{F_{n-1,n} + R_{n,n+1}}{1 + R_{n,n+1}F_{n-1,n}} \right] \tag{4}$$

where $F_{n-1,n} = \frac{f_{n-1}-f_n}{f_{n-1}+f_n}$ and $R_{n,n+1} = a_n^2(E_n^R/E_n)$.

The reflectivity at the interface between the air (or vacuum) and the film is obtained after previous determination of $R_{n-1,n}$ at all others interfaces inside the film, considering that $R_{N-1,N} = 0$, as the infinitely thick substrate does not add any reflection.

The electromagnetic radiation amplitude at each depth (z) inside a thin film can be determined in the same way by solving the equations 3 to inform the amplitude E_n at each layer n and depth z. Isolating E_n in equation 3 and using the value $R_{n-1,n} = a_{n-1}^2(E_{n-1}^R/E_{n-1})$, one straightforwardly obtains:

$$E_n = a_n a_{n-1} \left(\frac{1 + \frac{F_{n-1,n}+R_{n,n+1}}{1+R_{n,n+1}F_{n-1,n}}}{1 + R_{n,n+1}} \right) E_{n-1} \tag{5}$$

E_n can be recursively determined from the previous knowledge of the elements $R_{n,n+1}$ and $F_{n-1,n}$ calculated for the total reflectivity. Consequently, the amplitude at the upper interface of layer n is :

$$b_n = \frac{E_n}{a_n E_0} (1 + R_{n,n+1}) \tag{6}$$

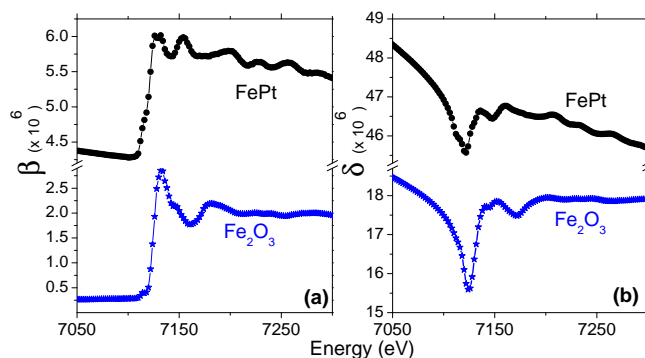with E_0 incident amplitude on the film surface ($n = 0$).

Fig. 1. (color online) Experimental refraction index $\hat{n} = 1 - \delta - i\beta$ corresponding to FePt and Fe_2O_3. In (a) is the imaginary β component, and the real δ component obtained with Kramers-Kronig transform is in (b).

The amplitude inside the layer n at an arbitrary position z_n relative to the top of the layer is then $B_n = b_n \cdot e^{-i\frac{2\pi}{\lambda} f_n z_n}$ and the radiation intensity inside this layer n is $I_n(z_n, \theta, E) = \left| b_n \cdot e^{-i\frac{2\pi}{\lambda} f_n z_n} \right|^2$. The total intensity $I(z, \theta, E)$ at each depth z is given by the set of $I_n(z_n, \theta, E)$ considering each thicknesses d_n and all possible n. The angle and energy dependences contained in the $f_n(\delta, \beta, \theta)$ complex terms are fully mathematicaly and computationally considered, where β and δ are the components of the refraction index, as shown in figure 1 for FePt and Fe_2O_3 compounds.

2.2. Depth dependence of XAS spectra

The electromagnetic radiation intensity $I(E, z, \theta)$ described above is used to determine the depth profile of XANES experimentally obtained in the grazing incidence geometry. This is performed by fitting XANES spectra for several grazing angles around the critical angle, considering the x-ray attenuation inside the material. The result of this process is the stratification in layers (of thickness dz) of the XANES information. The XANES spectra for each depth are fitted as a linear combination of reference spectral contributions previously determined. As the structure of layers inside the film can change dynamically in the fitting process, the $I(z, \theta, E)$ intensity must be calculated at each self-consistent fitting iteration.

To determine the depth dependence of μ_{exp}, it must be found a set of $\mu(E,z)$ data that when convoluted with $I(E,z,\theta)$ in the equation 1 simultaneously fits $\mu_{exp}(E,\theta)$ measured for several θ. This is more easily done rewriting the equation 1 in a discrete form considering the sum in z with steps of Δz in depth:

$$\mu_{exp}(E,\theta) = \frac{1}{\Gamma}\sum_{i=0}^{\infty} I(E,z_i,\theta)\mu(E,z_i) \tag{7}$$

where $z_0 = 0$, $z_\infty = \infty$, $z_{i+1} - z_i = \Delta z$ and $\Gamma = \sum_{i=0}^{\infty} I(E,z_i,\theta)$.

It is easily seen that the proportional contribution (PC) for each Δz layer at depth z_i for the signal $\mu_{exp}(E,\theta)$ is determined by $PC(z_i) = I(E,z_i,\theta)/\Gamma$. If the experimental spectra can be considered as a linear combination of several independent contributions of XANES features, $\mu_{exp}(E,\theta)$ can be considered as a linear combination of q spectral contributions (j) each one weighed by a factor w_j:

$$\mu_{exp}(E,\theta) = \frac{1}{\Pi}\sum_{j=1}^{q} \mu_j(E)\cdot w_j(\theta) \tag{8}$$

where Π is the normalization factor $\Pi = \sum_{j=1}^{q} w_j(\theta)$.

Considering the equations 7 and 8, each $\mu(E,z_i)$ can be written as $\mu(E,z_i) = \frac{1}{\Pi}\sum_{j=1}^{q} \mu_j(E)\cdot w_j(z_i)$ where $\Pi(z_i) = \sum_{j=1}^{q} w_j(z_i)$. Therefore:

$$\mu_{exp}(E,\theta) = \frac{1}{\Gamma}\sum_{i=0}^{\infty}\frac{1}{\Pi}\sum_{j=1}^{q} I(E,z_i,\theta)\cdot \mu_j(E)\cdot w_j(z_i) \tag{9}$$

The objective of determining all absorption contributions ($\mu_j(E)$) and its equivalent weight ($w_j(z_i)$) for each depth z_i can be achieved by fitting the experimental spectra $\mu_{exp}(E,\theta)$ with equation 9. Is important to note that since $\beta(E)$ for each spectral contribution at each layer is included on both $I(E,z,\theta)$ and $\mu(E,z)$ of equation 7, the deconvolution of $\mu_{exp}(E,\theta)$ must be a self-consistent procedure in terms of β. In other words, $I(E,z,\theta)$ must be computed at every iteration of the $\mu_{exp}(E,\theta)$ fitting procedure.

3. Application: depth profile in a FePt magnetic thin film

The FePt film studied here was grown by sputtering from pure targets of elemental Fe and Pt. It was deposited on MgO(100) substrate, which has normally a regular rough surface (in our case about 7 nm RMS). During the Fe and Pt deposition, the substrate temperature was kept at 500°C to ensure a high degree of chemical order and a perpendicular magnetic anisotropy (Martins *et al.*, 2006). It has been reported that, in these conditions, the growth is dominated by 3D islands surrounded by deep channels and a surface roughness reaching up to a few nanometers (Kim & Shin, 2001). Nevertheless, in our samples the substrate is previously covered with FCC Pt(100) buffer layer deposited at 500°C and consequently the surface roughness was considerably reduced. Atomic force microscopy (AFM) topographic measurements shows that, after buffer and sample depositions, the average roughness is of the order of 0.5 nm (figure 2). The composition and thickness of the film was checked by Rutherford Backscattering Spectroscopy confirming the equiatomic ratio (51% Fe and 49% Pt) and a thickness of 103 nm for the FePt layer.
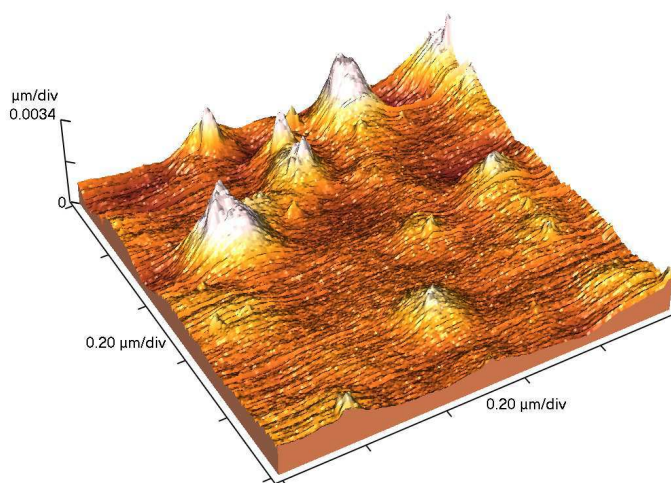

Fig. 2. (color online) Atomic force microscopy topographic measurement of a representative $1\mu m X 1\mu m$ area of the final grown sample. The surface roughness of the MgO (100) substrate is suppressed by covering it with a 50nm Pt (100) buffer deposited at 500°C. The final surface average roughness of the sample is 0.5nm.

When deposited at high substrate temperature (> 400°C) FePt thin films without cap layer protection are easily oxidized materials (Na *et al.*, 2001). The presence of a surface oxidation is clearly observed in the GI-XAS measurements at the smallest grazing angle presented on figure 3. The XANES features of this oxide layer was compared to many standard Fe oxides and could be identified as Fe_2O_3. The contribution of the oxide layer decreases rapidly for increasing angles, indicating that this layer is limited to a few Å. This is clearly seen by the decreasing (increasing) feature at 7133 (7115) eV and the shift of the spectra to lower energies presented in figure 3 (upper inset). For angles well above the critical angle, the XANES features come essentially from the FePt contribution.
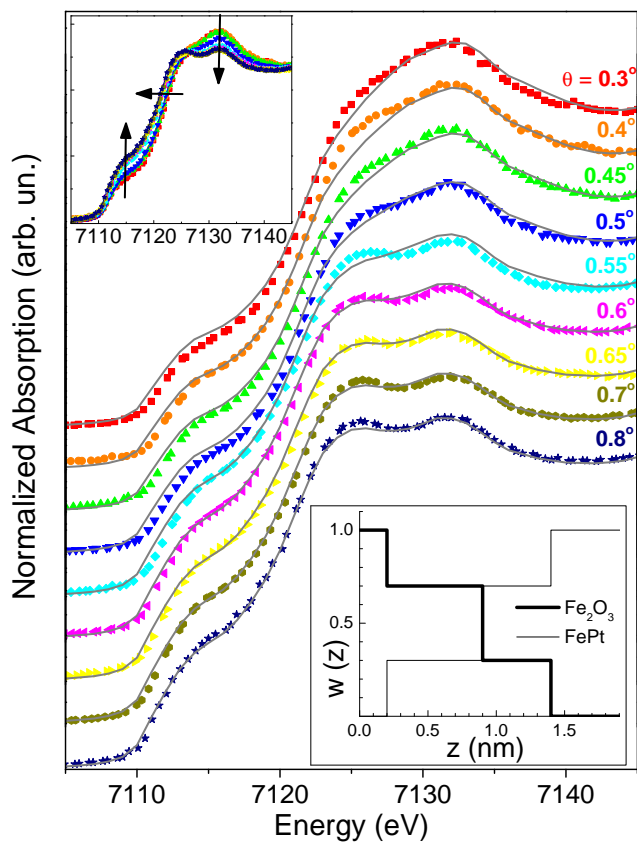
Fig. 3. (color online) Fitted XANES experimental data as a function of the energy and several grazing angles for a FePt film. The best model to fit the experimental data consists of a gradient between an oxidized surface with pure Fe_2O_3 layer (0.2 nm thick), with intermediary layers of both oxide and metal (0.7 and 0.5 nm thick), to the pure FePt metal inside the films. Upper inset : GI-XAS measurements for increasing grazing angles showing the dependence of the XANES features as a function of the penetration depth, or grazing angle. The arrows correspond to an increase in the grazing angle. Lower inset: weight function w for the two components (FePt and Fe_2O_3), for the oxidation profile corresponding to the best fit.
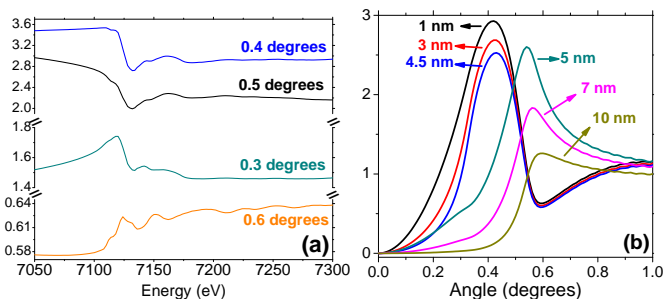
Fig. 4. (color online) Calculated intensity of the electromagnetic radiation inside a thin film of $[Fe_2O_3]_{5nm}/[FePt]_{95nm}/[Pt]_{50nm}/MgO$. In (a) is the intensity as function of photon energy and grazing angle, at fixed penetration of 2 nm. In (b) is the dependence with incident angle and the depth penetration, with fixed energy of 7130 eV.

Simple tabled or calculated δ and β components of the refraction index $\hat{n} = 1 - \delta - i\beta$ (Henke *et al.*, 1993; Chantler, 2000) cannot be used to calculate $I(E, z, \theta)$, given that it would include approximations not valid when the spectral features near a critical energy (absorption edge) are the desired information. The imaginary β component of the experimental refraction index was obtained for reference Fe_2O_3 and FePt samples using their absorption spectra scaled to tabled absolute values far from the absorption edges (Henke *et al.*, 1993; Chantler, 2000), as shown in figure 1a. Kramers-Kronig transforms(Ohta & Ishida, 1988; Bertie & Zhang, 1992; Peterson & Knight, 1973; Hoyt *et al.*, 1984; King, 2002; King, 2006; Cross & Frenkel, 1999) were used to determine the correspondent real δ component (fig. 1b). It was verified that taking reference XANES features for the fitting either from the same FePt film at the largest incident angle or from a standard sample gives equivalent results. To be consistent with the methodology, we choose to take both reference standard compound spectra, from the oxide and from the alloy, because, a priori, even extreme angle measurements are a mixture of both oxide and alloy compounds. Figure 4 shows the simulated intensity $I(E, z, \theta)$ for a model thick FePt film with a flat 5 nm Fe_2O_3 layer on its surface, using equation 6 and the refraction index data for each layer presented in figure 1. The XANES structures must definitively be taken into account when determining the experimental refraction index in order to include

all energy/angle dependences in $I(E, \theta)$, as is ratified by the strong non-linear dependence on $I(E)$ for different grazing angles shown in fig. 4a. The intensity $I(\theta)$ at $E = 7130\text{eV}$ for representative z values is shown in fig. 4b, which exemplifies multiple reflection interference effects near the critical angle for each penetration. The interference condition for the first Fe_2O_3 layer (5 nm) is drastically different from the resonances for the deeper layers, where the contributions arise essentially from the FePt alloy. These simulations emphasizes the strong need to consider all dynamical reflections at the interfaces to accurately calculate $I(E, z, \theta)$.

On the other hand it is worth noting that although corrections due to fluorescence self-absorption effects might be important in some cases, these effects are not significant for the angular range and penetration depth discussed here (<1% in the final error bars).

Equation 9, considering the iteratively determined $I(E, z, \theta)$, was used to simultaneously fit the experimental XANES spectra taken at several grazing angles (fig. 3). Reference XANES spectra of Fe_2O_3 and FePt were used in the fit.

The several experimental spectra simultaneously fitted, shown in figure 3, enable us to determine the complex layers structure in the depth profile, beyond a simply oxidized thickness determination. Different models of layers structure were considered for the oxidized FePt surface. Although a flat top oxide layer is well-suited to illustrate the general behavior, it is by far not the right solution to fit our data. The depth profile analysis shows clearly that the oxide not only covers the FePt film but penetrates beneath the film giving rise to a fractionated buried layer composed of the oxide and FePt. The best fit model turns out to be a gradient between a thin oxidized surface with pure Fe_2O_3 layer and intermediate layers of both oxide and metal alloy down to 1.4 nm from the surface. The top 100% oxide layer is 0.2 nm thick, followed by two mixed layers with 70% and 30% of Fe_2O_3 and 0.7 and 0.5 nm thick, respectively. The weight function w for each component is shown in the lower inset in figure 3.

It has been reported (Na *et al.*, 2001) that for FePt films an Fe oxide layer would form on the surface due to Fe migration to the oxide/metal interface during the growth at high

temperatures. As a result, there might be a composition variation with increasing film depth. In the metallic layer just below the oxide, Fe content should be lower than that of as-deposited film while Pt content should be higher. Our results confirm a compositional variation over the film depth, but supports a more complex picture. As known from literature(Kim & Shin, 2001), sputtered metallic films have some tendency to form pillars separated by deep channels. We interpret the gradient as resulting from the decoration of these pillars by the oxide that fills the empty space between pillars and oxidizes the very interfacial Fe atoms, rather than a continuous rough surface.

We have limited our analysis on the results based on the fluorescence data, which are much lesser sensitive to surface roughness effects compared to their reflectivity data counterpart. The penetration depth is the relevant parameter to fit the fluorescence datasets, and roughness would affect the accuracy in its determination. However, interface roughness contributions to the intensity of the electromagnectic wave inside the film still play an important role. As in the original Parrat's formalism (equation 4), roughness effects are not directly included in equations 5 and 6. Specifically to EXAFS in reflection mode, roughness effects have been treated by Keil and co-workers in a recent publication (Keil & Lutzenkirchen-Hecht, 2009). The inclusion of these effects are thoroughly considered in general reflectivity calculations using either a generalized approach to the distorted-wave Born approximation (Lee *et al.*, 2003) or a slicing procedure near the interfaces (Kravtsov *et al.*, 2009).

One main result coming from Keil et al (Keil & Lutzenkirchen-Hecht, 2009) is that the inclusion of roughness becomes necessary when thickness start to be bigger than 1 to 2 nm. In the range of 0.5 nm, which is our case, the effect of roughness has little effect on the overall extracted parameters from EXAFS reflectivity. On top of that, it is straightforward to recognize the gradual evolution from Fe2O3 to FePt at its interface as a result of inter-face roughness introduced by the slicing procedure. In this regard, we must emphasize that interface roughness was indirectly included in our fitting procedure by the inclusion of this

gradient. The exclusion of this interface gradient would worsen the goodness of the fit (the reduced χ^2 would degrade from 0.0017 to 0.0025).

It is noteworthy we have systematically measured the near edge fluorescence and reflectivity signals simultaneously. Moreover, the procedure to mathematically determine the depth profile to fit the fluorescence (XANES) datasets requires the calculation of the reflected intensity using equation 4. In this regard, figure 5 presents the experimental specular reflectivity near (absorption) edge spectra at three representative grazing angles together with their respective calculated spectra.We were not particularly interested in the reflectivity data, which were monitored by ionization chambers and not optimized in terms of signal-to-noise ratio. Despite the facts that surface roughness was not included in these reflectivity calculations and that it represents the most critical scenario to the theory (close to the critical angle and near an absorption edge) we obtain a fair agreement between experiment and theory. The fitting procedure described in the previous sections can be performed to simultaneously match both fluorescence and reflectivity experimental data to their corresponding calculations. However, since the pillars-like topography of this specific film is difficult to accurately model in terms of roughness, only the fluorescence data were considered in the goodness of the fit criteria.
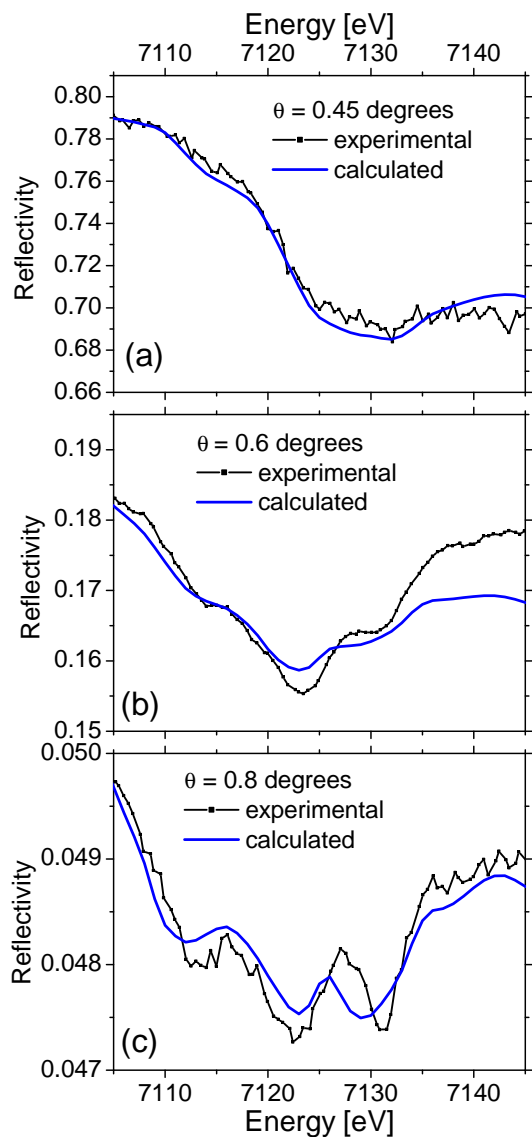
Fig. 5. Experimental and calculated specular reflectivity near edge spectra at three representative grazing angles.

Lateral roughness is of main importance when an off-specular geometry is used (Keil *et al.*, 2005), but usually insignificant for the specular reflectivity (Lee *et al.*, 2003; Kravtsov *et al.*, 2009). The lateral characteristic wavelength of the roughness may be estimated from figure 2, giving the characteristic peak-to-valley separation to be of the order of 200 nm. If we consider the average roughness to be 0.5 nm, this gives an average deviation angle of 2.5

mrad, or 0.14 degrees. Such an incident angular spread will impose a convolution of different angular contributions and lead to a decreased angular (or depth profile) resolution.

We should finally include an additional remark about the resolution of the depth profiles. Due to the exponential decay of the radiation intensity inside the film, the depth probed and final resolution of the method are intrinsically correlated and strongly dependent to the contrast between the refraction index of each layer material in the film. For instance, in the Fe_2O_3/FePt case the refraction index of Fe_2O_3 is factor three smaller than for the FePt material. In this case the profile variation is confined within 2 nm near the surface and the depth resolution is of order of one angstrom. If the compositional gradient were deeper into the film, the profile resolution would be lower for the internal layers.

4. Conclusion

Scattering and absorption phenomena are intrinsically intercorrelated when grazing incidence reflection and refraction are combined to x-ray absorption spectroscopy. The approach of GI-XAS presented in this article fully considers both scattering and absorption formalism for depth profiling the atomic, electronic or chemical local structures in thin films with nanometric resolution and limited roughness. This formalism can be applied to deconvolve the depth dependencies of not only XANES information as exemplified here, but also XRF (x-ray fluorescence) signals. It can be improved to take into account magnetic properties to handle XMCD (x-ray magnetic circular dichroism) signals in the fluorescence or reflectivity channels from thin films and multilayers, as it has already been done in the soft X-ray domain (Valencia *et al.*, 2008). This method can be directly applied for smooth surfaces and has advantage of being free of approximations in the formalism and of providing accurate depth profiling of the structure. It relies on accurate fluorescence (and reflectivity) measurements from which are derived its sensibility and accuracy.

from CNPq and CAPES.

References

Als-Nielsen, J. & McMorrow, D. (2001). *Elements of Modern X-ray Physics*. John Wiley and Sons.

Authier, A. (2001). *Dynamical Theory of X-Ray Diffraction*. Oxford University Press.

Baron, A. Q. R. (1995). *Resonant nuclear scattering of synchrotron radiation: detector development and specular scattering from a thin layer of* ^{57}Fe. Ph.D. thesis, Stanford University.

Bedzyk, M. J., Bommarito, G. M. & Schildkraut, J. S. (1989). *Phys. Rev. Lett.* **62**, 1376–1379.

Bertie, J. E. & Zhang, S. L. (1992). *Can. J. Chem.* **70**, 520–531.

Born, M. & Wolf, E. (1993). *Principles of Optics: Electromagnetic theory of propagation, interferenceand diffraction of light*. Pergamon Press.

Borthen, P. & Strehblow, H.-H. (1995). *Phys. Rev. B*, **52**, 3017–3019.

Chakalian, J., Freeland, J. W., Habermeier, H.-U., Cristiani, G., Khaliullin, G., van Veennedall, M. & Keimer, B. (2007). *Science*, **318**, 1114.

Chantler, C. T. (2000). *J. Phys. Chem. Ref. Data*, **29**, 597–1048.

Cross, J. O. & Frenkel, A. I. (1999). *Rev. Sci. Instrum.* **70**, 38–40.

deBoer, D. K. G. (1991). *Phys. Rev. B*, **44**, 498–511.

Heald, S. M., Chen, H. & Tranquada, J. M. (1988). *Phys. Rev. B*, **38**, 1016–1027.

Henke, B. L., Gullikson, E. M. & Davis, J. C. (1993). *Atomic Data and Nuclear Data Tables*, **54**, 181–342.

Hoyt, J. J., DeFontaine, D. & Warburton, W. K. (1984). *Journal Of Applied Crystallography*, **17**, 344–351.

Johnson, M. T., Bloemen, P. J. H., den Broeder, F. J. A. & de Vries, J. J. (1996). *Rep. Prog. Phys*, **59**, 1409–1458.

Keil, P. & Lutzenkirchen-Hecht, D. (2009). *Journal of Synchrotron Radiation*, **16**, 443–454.

Keil, P., Lutzenkirchen-Hecht, D. & Frahm, R. (2005). *Europhysics Letters*, **71**, 77–83.

Kim, M.-G. & Shin, S.-C. (2001). *J. Appl. Phys.* **90**, 2211.

King, F. W. (2002). *J. Opt. Soc. Am. B*, **19**, 2427–2436.

King, F. W. (2006). *Journal Of Physics A-Mathematical And General*, **39**(33), 10427–10435.

Kravtsov, E., Haskel, D., te Velthuis, S. G. E., Jiang, J. S. & Kirby, B. (2009). *Phys. Rev. B*, **79**, 134438.

Lee, D. R., Sinha, S. K., Haskel, D., Choi, Y., Lang, J. C., Stepanov, S. A. & Srajer, G. (2003). *Physical Review B*, **68**, 224409.

Martins, A., Fantini, M. C. A., Souza-Neto, N. M., Ramos, A. Y. & Santos, A. D. (2006). *J. Magn. Magn. Mat.* **305**, 152–156.

Mikulík, P. (1997). *X-ray reflectivity from planar and structured multilayers*. Ph.D. thesis, Univerité Joseph Fourier - Grenoble I.

Na, K., Na, J., Kim, H., Jang, P. & Lee, S. (2001). *IEEE TRANSACTIONS ON MAGNETICS*, **37**, 1302–1305.

Ohta, K. & Ishida, H. (1988). *Applied Spectroscopy*, **42**, 952–957.

Parrat, L. G. (1954). *Phys. Rev.* **95**, 359–369.

Peterson, C. W. & Knight, B. W. (1973). *Journal Of The Optical Society Of America*, **63**(10), 1238–1242.

Souza-Neto, N. M., Haskel, D., Tseng, Y. C. & Lapertot, G. (2009). *Phys. Rev. Lett.* **102**, 057206.

Souza-Neto, N. M., Ramos, A. Y., Tolentino, H. C. N., Martins, A. & Santos, A. D. (2006). *Appl. Phys. Lett.* **89**, 111910.

Stepanov, S. A., Kondrahkina, E. A., Kohler, R., Novikov, D. V., Materlik, G. & Durbin, S. M. (1998). *Physical Review B*, **57**, 4829–4841.

Stragier, H., Cross, J. O., Rehr, J. J., Sorensen, L. B., Bouldin, C. E. & Woicik, J. C. (1992). *Phys. Rev. Lett.* **69**, 3064–3067.

Tolentino, H. C. N., Ramos, A. Y., Alves, M. C. M., andE. Tamura, R. A. B., Cezar, J. C. & Watanabe, N. (2001). *J. Synchrotron Rad.* **8**, 1040–1046.

Valencia, S., Gaupp, A., Gudat, W., Abad, L., Balcells, L. & Martinez, B. (2008). *J. Appl. Phys.* **104**, 023903.

Weller, D. & Doemer, M. F. (2000). *Annual Review of Material Science*, **30**, 611–644.

Yun, W. B. & Bloch, J. M. (1990). *J. Appl. Phys.* **68**, 1421–1428.